Soft Matter

Plateau-Rayleigh instability in a soft viscoelastic material

Journal:	*Soft Matter*
Manuscript ID	SM-ART-01-2021-000019.R2
Article Type:	Paper
Date Submitted by the Author:	24-Feb-2021
Complete List of Authors:	Tamim, Saiful; Clemson University, Mechanical Engineering Bostwick, Joshua; Clemson University, Mechanical Engineering

Soft Matter

ARTICLE TYPE

Cite this: DOI: 00.0000/xxxxxxxxxx

Plateau-Rayleigh instability in a soft viscoelastic material

S. I. Tamim[a] and J. B. Bostwick*[a]

Received Date
Accepted Date

DOI: 00.0000/xxxxxxxxxx

A soft cylindrical interface endowed with surface tension can be unstable to wavy undulations. This is known as the Plateau-Rayleigh instability (PRI) and for solids the instability is governed by the competition between elasticity and capillarity. A dynamic stability analysis is performed for the cases of a soft i) cylinder and ii) cylindrical cavity assuming the material is viscoelastic with power-law rheology. The governing equations are made time-independent through the Laplace transform from which a solution is constructed using displacement potentials. The dispersion relationships are then derived, which depend upon the dimensionless elastocapillary number, solid Deborah number, and compressibility number, and the static stability limit, critical disturbance, and maximum growth rate are computed. This dynamic analysis recovers previous literature results in the appropriate limits. Elasticity stabilizes and compressibility destabilizes the PRI. For an incompressible material, viscoelasticity does not affect stability but does decrease the growth rate and shift the critical wavenumber to lower values. The critical wavenumber shows a more complex dependence upon compressibility for the cylinder but exhibits a predictable trend for the cylindrical cavity.

1 Introduction

Surface tension arises from molecular interactions at the interface between two immiscible materials. For liquids, surface tension forces dominate the response, i.e. flow, when the length scale of the system L is smaller than the capillary length $\ell_c = \sqrt{\sigma/\rho g}$, $L < \ell_c$, where σ is the surface tension, ρ the density and g the gravitational constant. The literature for these capillary flows is vast and well-studied in the fluid mechanics community. Solids also possess a surface tension[1,2], but this is often neglected as elasticity typically dominates the response for most common materials, e.g. metals or ceramics. Surface tension becomes important in solids when L is smaller than the elastocapillary length $\ell_e \equiv \sigma/E$, $L < \ell_e$, where E is the elastic modulus, and studies of such systems belong to the field of elastocapillarity[3,4]. Many soft gels have $E \sim 10$Pa, such that $\ell_e \sim 1$mm, and it is therefore unsurprising that many classical capillary instabilities have been observed in soft solids, such as the buoyancy-driven Rayleigh-Taylor instability[5,6], the Saffman-Taylor instability[7], parametrically-excited Faraday waves[8], and drop oscillations[6,9]. In this paper, we analyze the Plateau-Rayleigh instability of a soft viscoelastic cylinder.

A liquid cylinder will breakup into droplets due to surface tension, as is commonly seen in a dripping faucet. Plateau[10] used a static energy analysis to show that a cylinder with length longer than its circumference is unstable. This is the Plateau limit. This static analysis, however, is unable to predict the final drop size and associated wavelength of the instability. It was Rayleigh[11,12], who used a dynamic stability analysis to give a dispersion relationship that was able to determine the wavenumber with fastest growth rate and correctly predict the final drop size. For this reason, this has come to be known as the Plateau-Rayleigh instability, hereafter simply referred to as PRI.

Mora *et al.*[13] have observed PRI in soft agar gels using a novel experimental approach in which gel cylinders are cast in polystyrene molds are then immersed in toluene, which dissolves the mold and allows the instability to develop. Here they observe permanent undulations of the cylinder, but not complete breakup into drops, when $\ell_e/R > 6.2$. They perform a static stability analysis for a linear elastic cylinder to correctly predict this limit. Note that this is similar to the approach of Plateau. We use a dynamic analysis to predict the dispersion relationship from which the critical wavenumber of maximum growth rate is obtained, as it depends upon elastocapillarity, viscoelasticity, and compressibility. In this sense, our work is complementary to that of Mora *et al.*[13] in the same way that Rayleigh's dynamic analysis complemented the static analysis of Plateau.

PRI in soft solids is of interest to 3D bioprinting technologies[14?] and nonstandard inkjet[15], patterning of microfluidic devices[16,17], and pathologies related to biological tubes[18,19]. PRI in solids is different from fluids in that the competition between elastic and capillary energy can give rise to stable corrugated patterns[20–23]. This can be viewed as a phase separation between different regions of stretch that forms the beads-on-a-string structure due to PRI[24–26]. The cylindrical cavity is the complementary problem to the cylinder and has also received some attention recently[27–29]. We analyze both the cylinder and cylindrical cavity

Department of Mechanical Engineering, Clemson University, Clemson, SC 29634, USA. E-mail: jbostwi@clemson.edu

in this work.

Soft materials often exhibit a complex rheology and are characterized as viscoelastic materials with both an elasticity and viscosity, which are often frequency dependent[30,31]. Gels are one class of soft material that typically consists of a cross-linked polymer network that generally behaves as a solid with tunable elasticity[32]. The crosslinking networks present in these materials exhibit stress relaxation behaviour over a finite timescale which is typical of viscoelastic solids[33]. This viscoelastic relaxation of hydrogels can be manipulated to mimic behaviour of muscle tissues[34]. During 3D bioprinting, viscoelasticity of bioinks are known to affect the printability and structural integrity[35]. They are also used in creating biopolymers for numerous medical applications[36]. Polyacrylamide microgels are used to 3D print extracellular matrices[37], while PDMS have recently seen its use in 3D printing active structure that responds to external stimuli[38]. Commonly used soft hydrogels like agarose behave essentially as a linear elastic material for small strains[39] and has a capillary effect that is comparable to the bulk elasticity[9]. Materials with a more complex rheology can exhibit more complex behaviors that lead to experimentally-observed stick-slip motions during the spreading of a liquid over a soft material[40,41]. Here viscous, elastic, and capillary forces are all of similar magnitude[42]. Notably, Karpitschka *et al.*[43] have developed a model for a moving contact-line over a viscoelastic substrate recovering these stick-slip motions. These models are based on viscoelastic solids like PDMS that follow a power-law rheology with the characteristic viscoelastic timescale being in the range of $0 \sim 1$ seconds. In our model development, we take a similar approach and assume the soft viscoelastic material behaves as a power-law gel which admits a characteristic time scale that becomes zero in the purely elastic limit[44,45]. Viscoelastic fluids are also characterized with a slow relaxation timescale which increases with elasticity[46]. In this work we choose the capillary timescale in line with recent viscoelastic modelling approaches[47], which allows us to compare our results to classical results of PRI.

We begin this paper by defining the governing equations for a soft viscoelastic i) cylinder and ii) cylindrical cavity in Section 2. A solution is constructed in Section 3 by introducing displacement potentials, which gives rise to a dispersion relationship that depends upon dimensionless numbers that define elastocapillary, viscoelastic, and compressibility effects. In Section 4, we show how the dispersion relationship and stability characteristics are affected by the dimensionless numbers and we note that we recover previous results in the appropriate limit. Lastly, we end with some concluding remarks and discuss future directions.

2 Formulation

Consider a cylindrical rod of radius R in a cylindrical coordinate system (r,θ,z), as shown in Figure 1(a). This soft material is characterized by a density ρ, Lamé parameters λ,μ, Poisson ratio ν, and the interface is endowed with a surface tension σ. Our analysis presented herein is sufficiently general such that it is straightforward to also consider the complementary case of the cylindrical cavity in a soft material, as shown in Figure 1(b). In what follows, we perform a parallel analysis of these two problems.

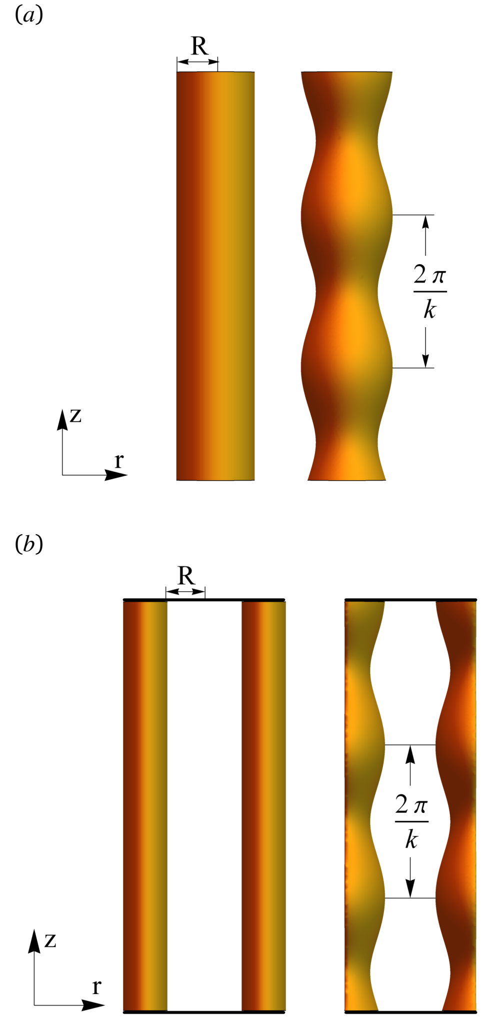

Fig. 1 Definition sketches for the soft (a) cylinder and (b) cylindrical cavity.

2.1 Field equations

The soft solid is assumed to be a linear viscoelastic material with the stress field τ_{ij} and strain field ε_{ij} related by[48],

$$\tau_{ij}(t) = 2\int_{-\infty}^{t} \mu(t-t')\frac{\partial \varepsilon_{ij}(t')}{\partial t'}dt' + \delta_{ij}\int_{-\infty}^{t} \lambda(t-t')\frac{\partial \varepsilon_{kk}(t')}{\partial t'}dt', \quad (1)$$

where $\mu(t)$ and $\lambda(t)$ are the relaxation moduli, which are related to one another through the Poisson ratio ν, $\lambda = 2\nu/(1-2\nu)\mu$. The strain field ε_{ij} is related to the displacement field $\mathbf{U}$,

$$\varepsilon_{ij} = \frac{1}{2}\left(\frac{\partial U_i}{\partial x_j} + \frac{\partial U_j}{\partial x_i}\right). \quad (2)$$

The equation of motion is given by Newton's second law

$$\frac{\partial \tau_{ij}}{\partial x_j} = \rho\frac{\partial^2 U_i}{\partial t^2}. \quad (3)$$

The jump in normal stress across the free surface boundary $r = R$ is given by the Young-Laplace equation and is proportional to the linearized curvature,

$$\tau_{rr}^e - \tau_{rr}^i = -\sigma\left(\frac{\partial^2 u_r}{\partial z^2} + \frac{u_r}{R^2}\right), \tag{4}$$

valid for small disturbances $u_r \ll 1$. Here i, e denote the inner and exterior material, respectively. For the cylinder $\tau^e = 0$, whereas for the cylindrical cavity $\tau^i = 0$. Continuity of shear stress is also enforced,

$$\tau_{rz} = \tau_{r\theta} = \tau_{z\theta} = 0. \tag{5}$$

2.2 Normal modes

Normal modes e^{st} are assumed with s is the growth rate, e.g. the displacement field is defined as $\mathbf{U} = \mathbf{u}(r,\theta,z)$ with $\mathbf{u}(r,\theta,z) = u_r(r,\theta,z)\hat{e}_r + u_\theta(r,\theta,z)\hat{e}_\theta + u_z(r,\theta,z)\hat{e}_z$ the time-independent field. We choose to work with the growth rate s instead of the frequency ω because our focus is on instability $s > 0$. We take the following Laplace transform,

$$f(s) = \int_0^\infty f(t)e^{-st}dt \tag{6}$$

and apply it to the constitutive relationship (1) to get,

$$\tilde{\tau}_{ij}(s) = 2\tilde{\mu}(s)\tilde{\varepsilon}_{ij}(s) + \delta_{ij}\tilde{\lambda}(s)\tilde{\varepsilon}_{kk}(s), \tag{7}$$

where the complex shear modulus $\tilde{\mu}(s)$ is defined as,

$$\tilde{\mu}(s) = \tilde{\mu}'(s) + i\tilde{\mu}''(s) = s\int_0^\infty \Psi(t)e^{-st}dt. \tag{8}$$

Here $\tilde{\mu}'(s)$ and $\tilde{\mu}''(s)$ are the storage and loss modulus, respectively, and Ψ is the relaxation function which is determined by the rheology of the material. For a complex solid, they are both a function of the frequency, or in our particular case, unstable growth rate. In most cases, the Poisson ratio ν is considered to be constant and independent of the frequency and therefore $\lambda = 2\mu\nu/1-2\nu$. Using (7) and the normal mode solution, the governing equation (3) can be written as

$$(\tilde{\lambda}(s) + \tilde{\mu}(s))\nabla(\nabla\cdot\mathbf{u}) + \tilde{\mu}(s)\nabla^2\mathbf{u} = \rho s^2\mathbf{u}. \tag{9}$$

The boundary conditions (4) & (5) have no explicit time dependence and follow similarly.

2.3 Rheology of soft gels

To solve (9) requires knowledge of the rheology of the viscoelastic solid, i.e. $\lambda(s)$ and $\mu(s)$[49]. The simplest models of viscoelasticity are the Maxwell model and the Kelvin-Voigt model. The former is more applicable to fluids while the latter is typically applied to solids. However, these single spring-dashpot model do not capture the wide ranging viscoelastic behavior of complex solids. Many soft solids consist of cross-linked polymers and are typically known as power law gels where $\mu'(s)$ and $\mu''(s)$ both scale with time as t^{-n}[44,45]. Here, n is the power law exponent and its value typically ranges from $0.5 \sim 1$ based on the stoichiometry of the polymer mixture. For these materials, the complex modulus is given by

$$\tilde{\mu}(s) = \mu_o\left(1 + (i\omega t_v)^n\right) \tag{10}$$

Here, μ_o is the static or reference shear modulus and t_v is a viscoelastic timescale. Note $i\omega$ is the complex frequency which is the same as the unstable growth rate, i.e., $s = i\omega$. Also, $t_v = 0$ corresponds to the purely elastic limit. The $n = 1$ case corresponds to the Kelvin-Voigt limit, in which the term $\mu_o t_v$ becomes the solid viscosity. For this reason (10) is somethimes referred to as as the fractional Kelvin-Voigt model[50]. Other fractional models have been put forth[51] and it would be straightforward to analyze these cases by simply substituting the functional form of $\tilde{\mu}$ in (9).

3 Solution

We construct a solution to (9) by introducing the potential functions $(\Phi, \mathbf{F})$ and using the Helmholtz decomposition of the displacement field,

$$\mathbf{u} = \nabla\Phi + \nabla\times\mathbf{F}. \tag{11}$$

Here Φ is a scalar potential and $\mathbf{F}$ is a vector potential. Applying (11) to (9) results in a set of decoupled Helmholtz equations,

$$\nabla^2\Phi - \alpha^2\Phi = 0 \tag{12a}$$

$$\nabla^2\mathbf{F} - \beta^2\mathbf{F} = 0. \tag{12b}$$

Here, $\alpha = s\sqrt{\frac{\rho}{\tilde{\lambda}+2\tilde{\mu}}}$ and $\beta = s\sqrt{\frac{\rho}{\tilde{\mu}}}$. The general solution of (12) is given by

$$\Phi(r,z) = A_0 I_0(r\sqrt{\alpha^2+k_z^2})e^{ik_z z} + B_0 K_0(r\sqrt{\alpha^2+k_z^2})e^{ik_z z}, \tag{13a}$$

$$F_r(r,z) = A_r I_1(r\sqrt{\beta^2+k_z^2})e^{ik_z z} + B_r K_1(r\sqrt{\beta^2+k_z^2})e^{ik_z z}, \tag{13b}$$

$$F_\theta(r,z) = A_\theta I_1(r\sqrt{\beta^2+k_z^2})e^{ik_z z} + B_\theta K_1(r\sqrt{\beta^2+k_z^2})e^{ik_z z}, \tag{13c}$$

$$F_z(r,z) = A_z I_0(r\sqrt{\beta^2+k_z^2})e^{ik_z z} + B_z K_0(r\sqrt{\beta^2+k_z^2})e^{ik_z z}, \tag{13d}$$

where we have assumed axisymmetry, i.e. no θ dependence, consistent with the Steiner symmetrization procedure which gives the most destabilizing disturbance[52,53]. Here, F_r, F_θ, F_z are the scalar components of $\mathbf{F}$, k_z is the wavenumber in the z-direction, and I and K are the modified Bessel functions of the first and second kind, respectively. The Bessel function I diverges at $r\to\infty$, while K diverges at $r \to 0$. Therefore, for the case of the cylinder we set $B_0 = B_r = B_\theta = B_z = 0$ and for cylindrical cavity we set $A_0 = A_r = A_\theta = A_z = 0$ to ensure a physical solution.

3.1 Nondimensionalization

We scale the lengths with undisturbed radius R and time with the capillary time scale $\sqrt{\rho R^3/\sigma}$. This gives rise to the following non-dimensional parameters,

$$k = k_z R,\quad \xi = s\sqrt{\frac{\rho R^3}{\sigma}},\quad \Sigma = \frac{\sigma}{\mu_o R},\quad \tau = t_v\sqrt{\frac{\sigma}{\rho R^3}},\quad \kappa = \sqrt{\frac{1-2\nu}{2(1-\nu)}},$$

$$\gamma_1 = \sqrt{\kappa^2\xi^2\tilde{\Sigma}+k^2},\quad \gamma_2 = \sqrt{\xi^2\tilde{\Sigma}+k^2}\quad \tilde{\Sigma} = \frac{\Sigma_0}{1+(\tau\xi)^n}. \tag{14}$$

Here, ξ is non-dimensional growth rate and k the scaled wavenumber. Three dimensionless numbers appear; κ is a compressibility number that ranges from $\kappa = 0$ for an incompressible $\nu = 0.5$ material to $\kappa = 1/\sqrt{2}$ for a fully compressible $\nu = 0$ material, τ is the solid Deborah number[54] that is a measure of the relaxation time of the material relative to the capillary time scale with $\tau = 0$ corresponding to the purely elastic limit, and Σ is the elastocapillary number representing the relative balance of capillary and elastic forces. Experiments using agarose gels have obtained softness up to $\Sigma \sim O(10)$[9,13], while thin columns of ultrasoft gels can have even higher Σ.

3.2 Dispersion equations

Applying the solution (13) to the boundary conditions (4,5) yields a set of linear equations for the unknown A's in the cylinder case and the unknown B's for the cylindrical cavity. The solvability condition for each case gives the corresponding dispersion relationship.

3.2.1 Solid cylinder

We begin with the case of the cylinder and write the boundary conditions (4) and (5) as

$$A_0\left(\frac{\gamma_2^2+k^2}{2}I_0(\gamma_1)-\gamma_1 I_1(\gamma_1)\right)-A_\theta ik\left(\gamma_2 I_0(\gamma_2)-I_1(\gamma_2)\right)$$

$$=A_0\frac{\tilde{\Sigma}}{2}(1-k^2)\gamma_1 I_1(\gamma_1)+A_\theta\frac{\tilde{\Sigma}}{2}ik(1-k^2)I_1(\gamma_2), \tag{15a}$$

$$A_0 2ik\gamma_1 I_1(\gamma_1)+A_\theta(\gamma_2^2+k^2)I_1(\gamma_2)=0, \tag{15b}$$

$$A_r(ik)\left(\gamma_2 I_0(\gamma_2)-2I_1(\gamma_2)\right)-A_z\left(\gamma_2^2 I_0(\gamma_2)-2\gamma_2 I_1(\gamma_2)\right)=0, \tag{15c}$$

$$A_r k I_1(\gamma_2)+A_z i\gamma_2 I_1(\gamma_2)=0. \tag{15d}$$

Note that (15a,15b) and (15c,15d) are decoupled and admit two classes of solution. Our focus is on the shape change modes which are described by Equations (15a,15b), whose solvability condition generates the dispersion relationship

$$\begin{aligned}&2k^2\gamma_1\gamma_2 I_0(\gamma_2)I_1(\gamma_1)-\frac{1}{2}(\gamma_2^2+k^2)^2 I_0(\gamma_1)I_1(\gamma_2)\\&+\left(1+\frac{\tilde{\Sigma}}{2}(1-k^2)\right)\gamma_1(\gamma_2^2-k^2)I_1(\gamma_1)I_1(\gamma_2)=0.\end{aligned} \tag{16}$$

3.2.2 Cylindrical cavity

Similarly, we can write the boundary conditions (4) and (5) for the cylindrical cavity as

$$B_0\left(\frac{\gamma_2^2+k^2}{2}K_0(\gamma_1)+\gamma_1 K_1(\gamma_1)\right)+B_\theta ik\left(\gamma_2 B_0(\gamma_2)+K_1(\gamma_2)\right)$$

$$=B_0\frac{\tilde{\Sigma}}{2}(1-k^2)\gamma_1 K_1(\gamma_1)+B_\theta\frac{\tilde{\Sigma}}{2}ik(1-k^2)K_1(\gamma_2), \tag{17a}$$

$$B_0 2ik\gamma_1 K_1(\gamma_1)-B_\theta(\gamma_2^2+k^2)K_1(\gamma_2)=0, \tag{17b}$$

$$B_r(ik)I_0(\gamma_2)+B_z\gamma_2 I_0(\gamma_2)=0, \tag{17c}$$

$$B_r k I_1(\gamma_2)-B_z i\gamma_2 I_1(\gamma_2)=0. \tag{17d}$$

The solvability condition for the shape modes (17a,17b) gives the dispersion relationship

$$\begin{aligned}&2k^2\gamma_1\gamma_2 K_0(\gamma_2)K_1(\gamma_1)-\frac{1}{2}(\gamma_2^2+k^2)^2 K_0(\gamma_1)K_1(\gamma_2)\\&-\left(1-\frac{\tilde{\Sigma}}{2}(1-k^2)\right)\gamma_1(\gamma_2^2-k^2)K_1(\gamma_1)K_1(\gamma_2)=0\end{aligned} \tag{18}$$

4 Results

The dispersion curve $\xi(k)$ can be computed numerically from (16) and (18) for the rod and cylindrical cavity, respectively. For reference, the dispersion relationship for the classical PRI is given by[11],

$$\xi^2=(1-k^2)k\frac{I_1(k)}{I_0(k)}, \tag{19}$$

which neglects both viscosity and elasticity. In what follows, we systematically investigate how the dispersion relationship depends upon the dimensionless numbers Σ, κ, τ, n focusing on the role of viscoelasticity. We start with the rod and begin by focusing on the purely elastic limit $\tau = 0$ before showing how viscoelasticity affects stability. We then analyze the cylindrical cavity highlighting the difference with the cylindrical rod.

4.1 Solid cylinder

Figure 2 plots the dispersion curves, growth rate ξ against wavenumber k, for a purely elastic $\tau = 0$ material illustrating the competing roles of elastocapillarity Σ and compressibility κ. Most soft gels are hydrogels that are comprised mainly of water such that they are incompressible $\kappa = 0$[39,55]. Figure 2(a) plots the dispersion curve for an incompressible material $\tilde{\nu} = 0$ for a range of elastocapillary numbers Σ. Each curve exhibits a range of unstable wavenumbers k_s that define the static limit $\xi = 0$ and a maximum growth rate ξ_m that occurs at a wavenumber k_m. In the limit $\Sigma \to \infty$, we recover the PRI as could be expected. Increasing the elasticity relative to surface tension corresponds to decreasing the elastocapillary number Σ, which is shown to be stabilizing in that both the maximum growth rate ξ_m and range of unstable wavenumbers k_s shrink. In contrast, increasing the compressibility κ is destabilizing, as shown in Figure 2(b). Note that the wavenumber of maximum growth k_m shifts to a long wave-

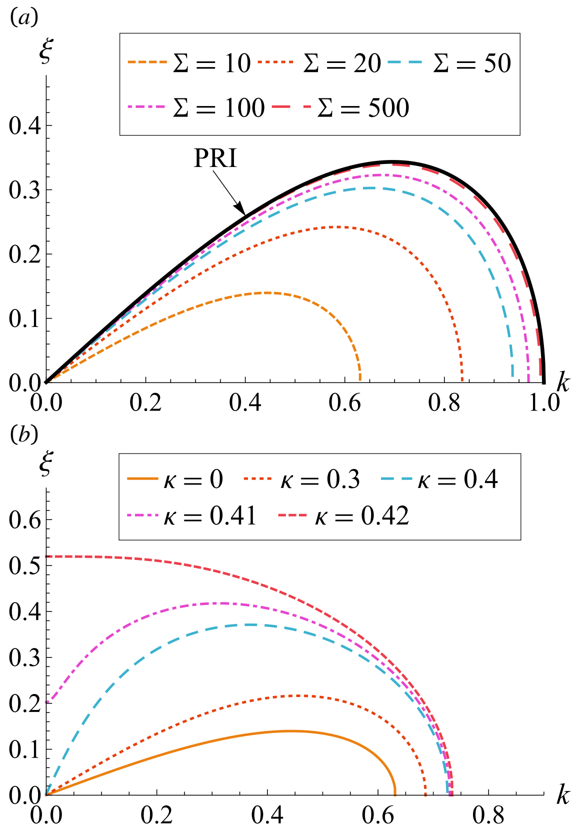

Fig. 2 Dispersion curves for a cylinder plotting growth rate ξ against wavenumber k for a purely elastic solid $\tau = 0$, as it depends upon (a) the elastocapillary number Σ for an incompressible $\kappa = 0$ material and (b) compressibility number κ for fixed $\Sigma = 10$. The solid line is the dispersion relation for the PRI, Eq. (19).

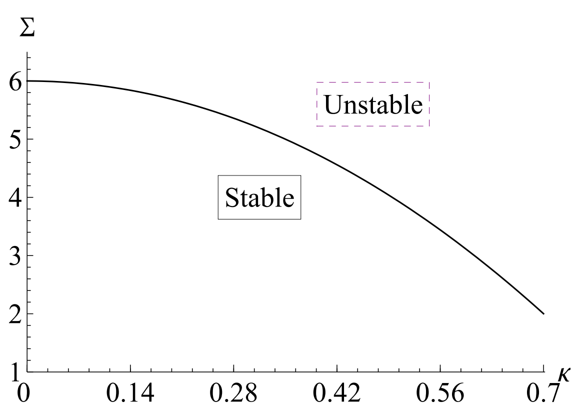

Fig. 3 Stability diagram for the purely elastic $\tau = 0$ cylinder in the parameter space defined by the elastocapillary Σ and compressibility κ numbers.

length $k_m = 0$ disturbance for a range of κ, which corresponds to a uniform shrinking or collapse of the cylinder due to capillarity.

The relative balance between stabilizing elasticity and destabilizing compressibility gives rise to the stability diagram shown in Figure 3 plotted in the $\Sigma - \kappa$ parameter space for a purely elastic material $\tau = 0$. Here the incompressible $\kappa = 0$ limit agrees with the static analysis of Mora *et al.*[13] which yields the threshold value $\Sigma = 6$. As the compressibility κ increases, the threshold value of elastocapillary number Σ decreases to $\Sigma = 2$ at $\kappa = 1/\sqrt{2}$. Notably, this limit has been reported as the instability threshold for the cylindrical cavity by Xuan *et al.*[27], which we discuss further shortly.

Although most gels used in experiment can be reasonably approximated to be incompressible materials, compressible gels might be useful to specific applications[56]. Compressibility can destabilize beyond the PRI limit. Figure 4 shows how the stability properties k_s, k_m, ξ_m are affected by the compressibility κ for a purely elastic $\tau = 0$ cylinder. The stability limit k_s is a monotonically increasing function κ, whereas the properties of the critical disturbance are more complex. The maximum growth rate ξ_m similarly increases monotonically with both Σ and κ, but the critical wavenumber displays a more complex dependence on Σ, κ. For large elastocapillary number $\Sigma = 20$, k_m monotonically decreases with κ until the long wavelength $k = 0$ limit is reached, whereas for small elastocapillary number $\Sigma = 7$, k_m increases with κ, reaches a maximum value and then rapidly decreases to $k = 0$. This highlights a complex interplay between surface tension, elasticity, and compressibility.

4.1.1 Viscoelasticity

Equation (19) is the PRI dispersion relationship for an inviscid liquid cylinder, which exhibits three main properties; 1) the most unstable wavenumber is $k_m = 0.697$, 2) the growth rate for the most unstable wavenumber is $\xi_m = 0.343$, and 3) the static stability limit is $k_s = 1$. This result is an upper bound for an incompressible elastic solid $\kappa = 0$, as elasticity is shown to be a stabilizing effect (cf. Figure 2(a)).

Viscoelasticity is also stabilizing and is described in our model by the Deborah number τ and exponent n. Figure 5 plots the dispersion relationship ξ against k, as it depends upon these viscoelastic properties. In Figure 5(a), we show that the growth rate ξ decreases and k_m shifts to lower wavenumbers as τ increases from the purely elastic limit $\tau = 0$. The effect of the exponent n is shown in Figure 5(b) with increased damping associated with decreasing n with the Kelvin-Voigt case $n = 1$ being the most unstable in this range of parameters. Note that the static stability limit k_s is unaffected by both τ and n (cf. Figure 5). That is, viscoelasticity damps the growth rate but does not change the range of unstable wavenumbers. The is further illustrated in Figure 6(a) which plots k_s against the elastocapillary number Σ showing that τ has not effect on the stability limit. However, τ does shift k_m to lower wavenumbers and decreases ξ_m, as shown in Figure 6(b) and Figure 6(c), respectively. Again, the $\Sigma \to \infty$ is the most unstable situation, regardless of τ and n.

The critical disturbance k_m and associated growth rate ξ_m are shown in Figure 7, as they depend upon the elastocapillary num-

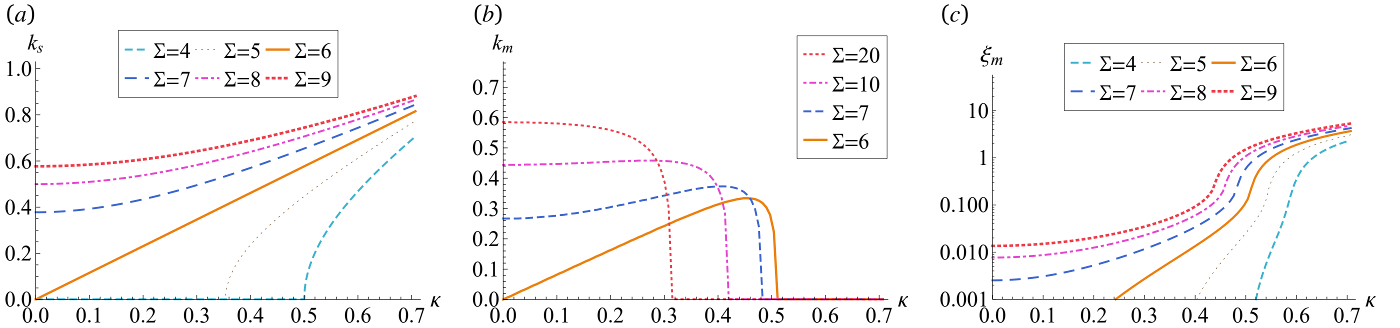

Fig. 4 Stability characteristics for a compressible purely elastic $\tau = 0$ cylinder plotting (a) the static stability limit k_s, (b) critical wavenumber k_m, and (c) maximum growth rate ξ_m against the compressibility κ, as it depends upon the elastocapillary number Σ.

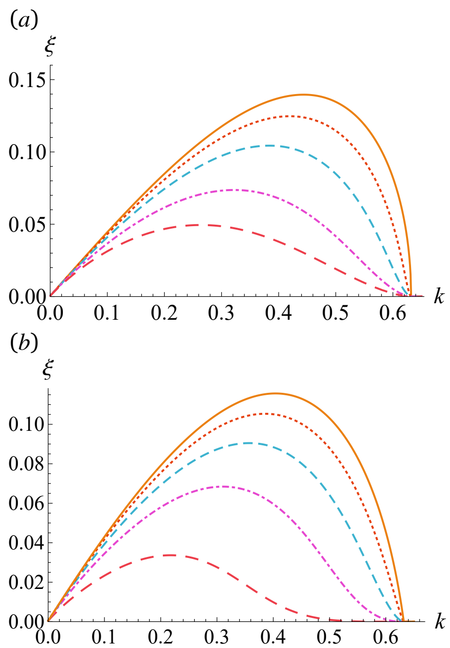

Fig. 5 Viscoelastic effects illustrated in the dispersion relationship plotting growth rate ξ against wavenumber k, as it depends upon (a) solid Deborah number τ $(\Sigma = 10, n = 0.5)$ and (b) exponent n $(\Sigma = 10, \tau = 1)$.

ber Σ and solid Deborah number τ. The trend is monotonic in both dimensionless numbers; the growth rate increases with i) increasing Σ and ii) decreasing τ. The same monotonic trends exist for variations in the exponent n.

4.2 Cylindrical cavity

Figure 8 plots the growth rate ξ against wavenumber k for a cylindrical cavity immersed in a purely elastic $\tau = 0$ material. For an incompressible material $\kappa = 0$, decreasing Σ, i.e. increasing elasticity, is stabilizing (cf. Figure 8(a)). In the capillary limit $\Sigma \to \infty$, the dispersion approaches the PRI limit for a cylindrical cavity,

$$\xi^2 = (1 - k^2)k\frac{K_1(k)}{K_0(k)}, \qquad (20)$$

which admits the stability characteristics, $k_s = 1, k_m = 0.484, \xi_m = 0.82$. For an incompressible material $\kappa = 0$, this is the most unstable situation. In contrast, for fixed Σ increasing the compressibility of the material is destabilizing (cf. Figure 8(b)). Interestingly, the static stability limit k_s is nearly unaffected by κ unlike the case of the cylinder (cf. Figure 2(b)). The stability boundary is given by $\Sigma = 2$ irrespective of κ and this agrees with previous literature[27].

Figure 9 plots the stability characteristics (k_s, k_m, ξ_m) for a purely elastic $\tau = 0$ cylindrical cavity against the compressibility κ. The static stability limit k_s shows a very weak dependence upon κ that increases with Σ (cf. Figure 9(a)). The critical wavenumber k_m decreases with increasing compressibility κ and eventually becomes $k_m = 0$ at a critical value of the compressibility κ^* which decreases with increasing Σ (cf. Figure 9(b)). The maximum growth rate ξ_m increases with both Σ and κ, as shown in Figure 9(c). Lastly, we note that the growth rate remains the same order of magnitude over the entire range of κ, unlike the cylinder whose growth rate varied substantially with κ (cf. Figure 4(c)).

4.2.1 Viscoelasticity

Similar to the cylinder, viscoelasticity affects the critical wavenumber k_m and growth rate ξ_m, but not the static stability limit k_s for the incompressible $\kappa = 0$ cylindrical cavity, as shown in Figure 10. Increasing the solid Deborah number τ shifts k_m to lower wavenumbers and decreases the growth rate for fixed Σ. In the limit $\Sigma \to \infty$, the PRI limit is approached and the effect of τ is negligible.

Figure 11 plots the critical disturbance k_m and associated growth rate ξ_m for the incompressible $\kappa = 0$ cylindrical cavity, as they depend upon the elastocapillary number Σ and solid Deborah number τ. The trend is monotonic in both dimensionless numbers; the growth rate increases with i) increasing Σ and ii) decreasing τ.

5 Comparison with experiment

Here we compare our results to the experimental data on capillary driven instability in solid cylinders by Mora *et al.*[13]. Their experiments were performed using thin cylinders ($R = 240\mu m$) of agar and show the emergene of an unstable wavy undulation along the axis of the cylinder. The instability disappeared with decreasing elastocapillary number $\Sigma < 6$, consistent with predictions from our model. For a cylinder with $\Sigma = 10.6$ (Mora *et al.* Figure 2d), they observed an unstable wavelength $\lambda \approx 30R$, which

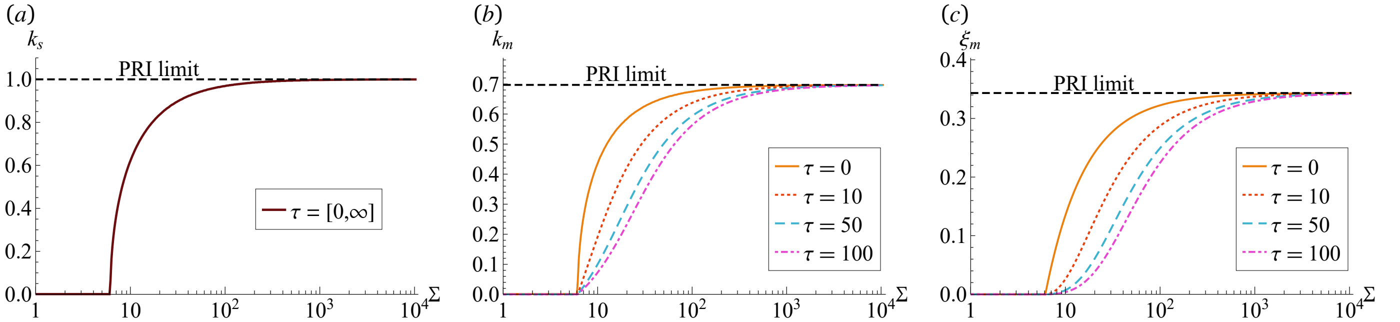

Fig. 6 Stability characteristics of an incompressible $\kappa = 0$ viscoelastic cylinder plotting the (a) static stability limit k_s, (b) critical wavenumber, and (c) maximum growth rate ξ_m against the elastocapillary number Σ, as it depends upon the solid Deborah number τ for $n = 0.5$. The dashed line denotes the PRI limit.

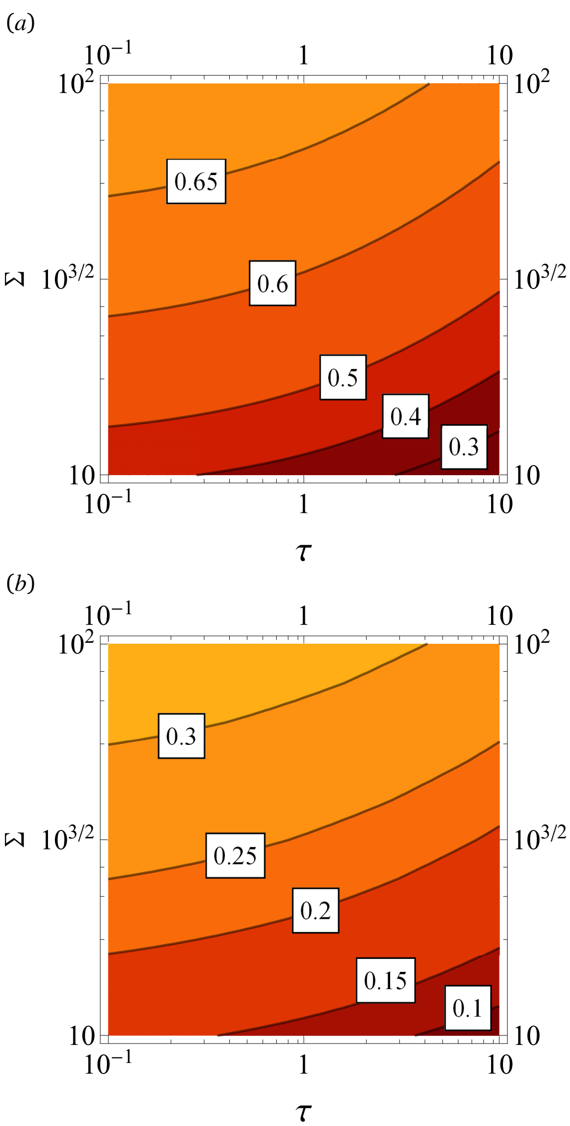

Fig. 7 Critical disturbance plotting (a) the wavenumber k_m and (b) growth rate ξ_m against the elastocapillary number Σ and solid Deborah number τ for an incompressible $\kappa = 0$ cylinder with $n = 0.5$.

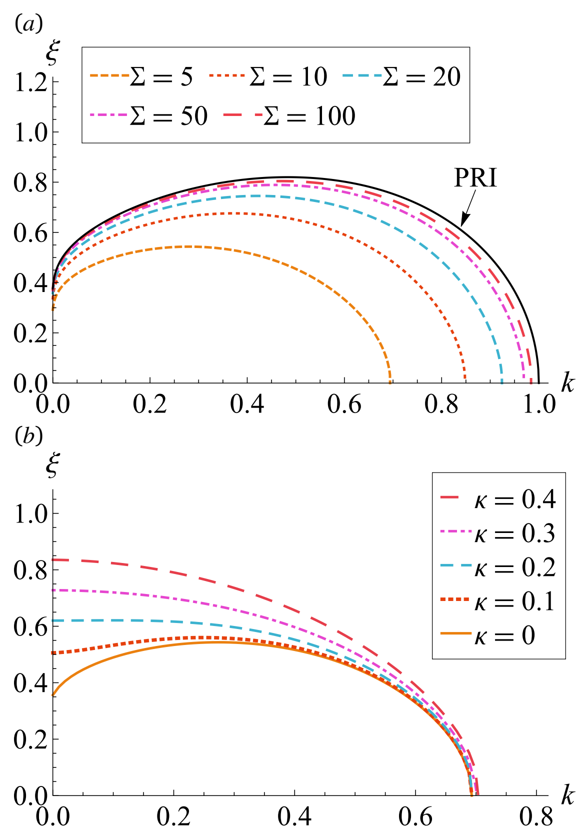

Fig. 8 Dispersion curves for a cylindrical cavity plotting growth rate ξ against wavenumber k, as it depends upon (a) the elastocapillary number Σ for $\kappa = 0$ and (b) compressibility number κ for $\Sigma = 5$. The solid line is the PRI dispersion for a cylindrical cavity given by Equation (20).

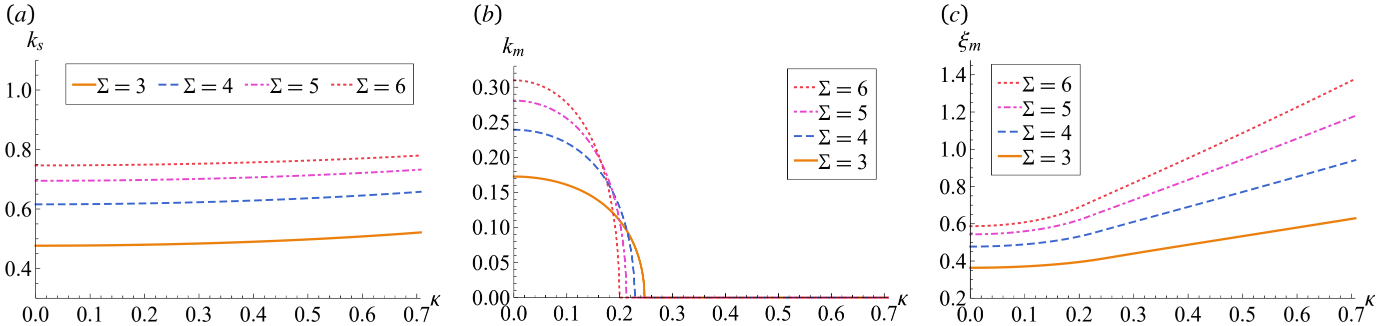

Fig. 9 Stability characteristics for a compressible purely elastic $\tau=0$ cylindrical cavity plotting (a) the static stability limit k_s, (b) critical wavenumber k_m, and (c) maximum growth rate ξ_m against the compressibility κ, as it depends upon the elastocapillary number Σ.

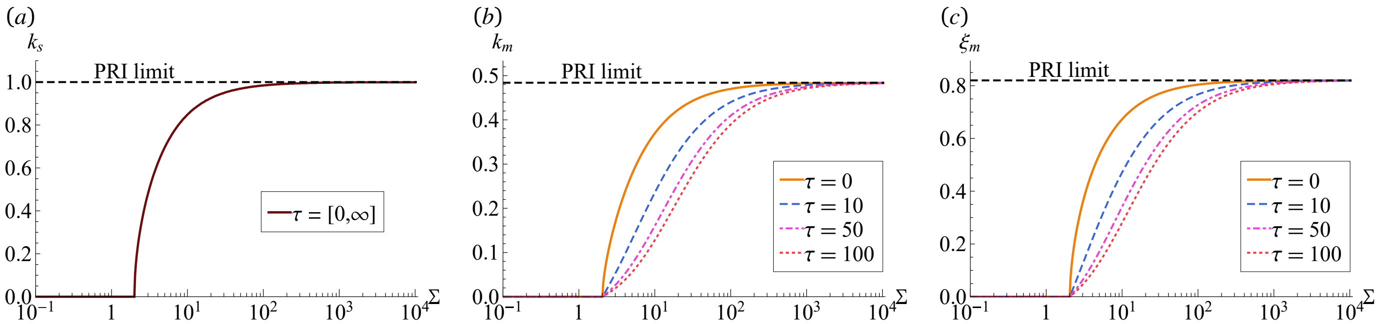

Fig. 10 Stability characteristics for an incompressible $\kappa=0$ cylindrical cavity plotting (a) the static stability limit k_s, (b) critical wavenumber k_m, and (c) maximum growth rate ξ_m against the elastocapillary number Σ, as it depends upon the solid Deborah number τ for $n=1$. Dashed line refer to the PRI limit.

is much longer than that predicted by Rayleigh's theory $\lambda \approx 9.1R$. This is presumably due to the elasticity of the agar gel. Our purely elastic solution ($\tau=0$) predicts wavelengths $\lambda \approx 13R$, longer than the Rayleigh limit, but still lower than experimental observation. We hypothesize that this discrepancy is due to a viscoelastic effect which shifts to longer wavelengths according to our model (cf. Figure 5). Even though the capillary time scale is small $\approx 10^{-3}$s, the non-dimensional viscoelastic relaxation time τ can be $O(1)$ for materials with short relaxation times, as is true for the agar gels used in the experiments by Mora *et al.* Figure 1. As shown in Figure 5, increasing τ leads to smaller k_m, i.e., longer critical wavelegths. Also, the Ohnesorge number ($Oh = \frac{G_o t_v}{\sqrt{\rho\sigma R}}$) corresponding to the parameters in the Mora experiment should be larger than 1. This shows the importance of including solid viscoelasticity in the dynamic stability analysis. If we assume a simple Kelvin-Voigt rheology ($n=1$) we can fit the observed wavelength from experiment for $\Sigma=10.6$ to our model when $\tau=5$. This shows the importance of including viscoelastic effects into the analysis to predict critical wavelength. Furthermore, a recent paper has also shown through numerical nonlinear analysis that the final modes are indeed selected by a dynamic process[23].

6 Concluding remarks

We have developed a model for the PRI in viscoelastic solids for the complementary geometries of the cylinder and cylindrical cavity. Dispersion relationships have been derived and depend upon the non-dimensional numbers Σ, τ, κ, which account for elastocapillary, viscoelasticity, and compressibility, respectively. Our dynamic model is distinguished in that we predict the critical wavenumber k_m of maximum growth rate ξ_m that should be observed in experiment, and we also recover the previously reported static stability results for the incompressible cylinder $\Sigma=6$[13] and incompressible cylindrical cavity $\Sigma=2$[27] by setting the growth rate $\xi=0$. This approach is similar to how Rayleigh's dynamic analysis[11] complemented the static analysis of Plateau[10] for the PRI. Both elasticity and viscoelasticity are stabilizing effects, whereas compressibility is destabilizing. For an incompressible material, viscoelasticity does not affect the range of unstable wavenumbers k_s, but does affect the critical disturbance by shifting k_m to lower wavenumbers and decreasing the growth rate ξ_m (cf. Figure 6,10). The effect of the power law exponent n is quantitative but does not qualitatively change our results. For a compressible material, the stability limit for Σ decreases with increasing κ for the cylinder, but is a constant $\Sigma=2$ for the cylindrical cavity and independent of compressibility. For the cylinder, compressibility increases the range of unstable wavenumbers k_s and increases the growth rate ξ_m, but the critical wavenumber k_m has a more complex dependence on Σ, κ, as shown in Figure 4. The associated trends for the cylindrical cavity are more monotonic (cf. Figure 9).

The classic PRI of an inviscid liquid sees the cylindrical jet breakup into spherical droplets in what are naturally large-amplitude disturbances. Soft solids tend to show nonlinear behavior at large strain[57] and this causes the PRI to assume an

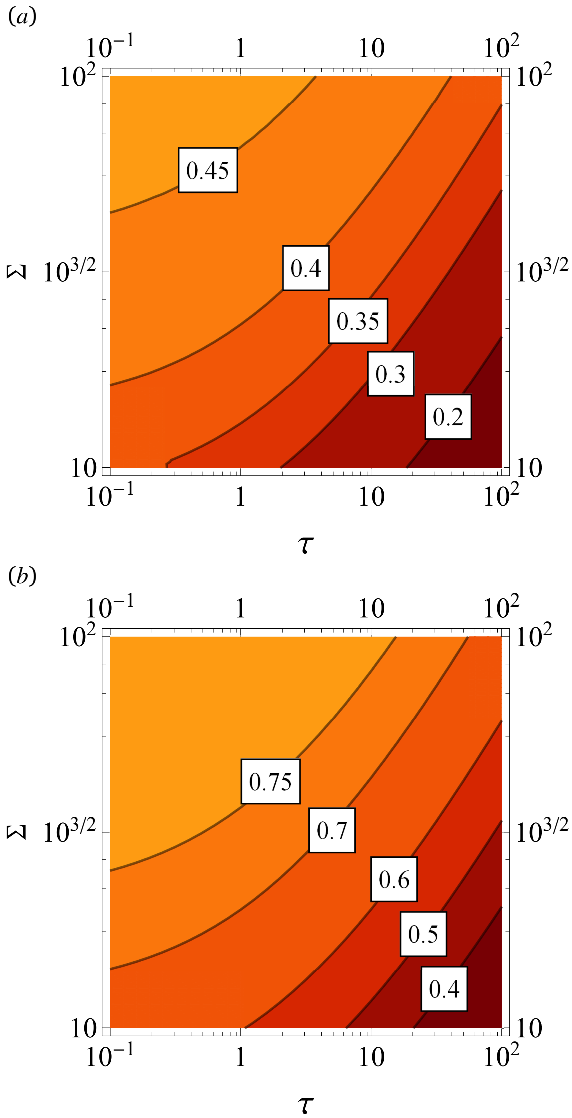

Fig. 11 Critical disturbance plotting (*a*) the wavenumber k_m and (*b*) growth rate ξ_m against the elastocapillary number Σ and solid Deborah number τ for an incompressible $\kappa = 0$ cylindrical cavity with $n = 0.6$.

undulating shape in experiment[13]. Our analysis assumes small strains, but still should be able to describe the instability mechanism, predict the stability limit, as well as the critical disturbance which often persists (i.e. the linear mode quenches itself) in weakly nonlinear analysis provided the bifurcation is supercritical[58]. Nevertheless, understanding the role of nonlinear elasticity and complex rheology of soft solids has seen sustained interest among researchers[?] . Yield stress materials behave elastically beyond the jamming transition threshold. This enhances the stability of 3D printed structures[59] pointing to a nonlinear response of the material. Future directions in the study of the PRI could focus on large strains in the nonlinear regime and how this affects the morphology of the instability. This will aid in developing fabrication techniques for soft solids, i.e. bioprinting, which exploit pattern formation, as these are naturally large amplitude disturbances. Lastly, the techniques developed here could be used to model other systems, e.g., soft tubes or channels of finite thickness filled with a flowing viscous fluid, that could shed light on other dynamic elastocapillary phenomena.

A Cylindrical components

The displacement and stress components required for derivation of the dispersion relations are obtained using general solutions in Equation (13).

A.1 Cylinder

The displacement components of a solid cylinder are,

$$u_r = (A_0 a I_1(ar) - A_\theta (ik_z) I_1(br))\, e^{ik_z z}, \tag{21a}$$

$$u_\theta = (A_r (ik_z) I_1(br) - A_z b I_1(br))\, e^{ik_z z}, \tag{21b}$$

$$u_z = (A_0 (ik_z) I_0(ar) + A_\theta b I_0(br))\, e^{ik_z z}, \tag{21c}$$

where $a = \sqrt{\alpha^2 + k_z^2}, b = \sqrt{\beta^2 + k_z^2}$. Using the constitutive relation (7), the stresses are obtained as

$$\tau_{rr} = 2\tilde{\mu} \left[A_0 \left(\frac{b^2 + k_z^2}{2} I_0(ar) - \frac{a}{r} I_1(ar) \right) - A_\theta (ik_z) \left(b I_0(br) - \frac{1}{r} I_1(br) \right) \right] e^{ik_z z}, \tag{22a}$$

$$\tau_{rz} = \tilde{\mu} \left[A_0 (ik_z) 2a I_1(ar) + A_\theta (b^2 + k_z^2) I_1(br) \right] e^{ik_z z}, \tag{22b}$$

$$\tau_{r\theta} = \tilde{\mu} \left[A_r (ik_z) \left(b I_0(br) - \frac{2}{r} I_1(br) \right) - A_z \left(b^2 I_0(br) - \frac{2b}{r} I_1(br) \right) \right] e^{ik_z z}, \tag{22c}$$

$$\tau_{\theta z} = \tilde{\mu} \left[-A_r k_z^2 I_1(br) - A_z b (ik_z) I_1(br) \right] e^{ik_z z}. \tag{22d}$$

A.2 Cylindrical cavity

Similarly for a hollow cylindrical cavity, the displacements components are

$$u_r = (-B_0 a K_1(ar) - B_\theta (ik_z) K_1(br))\, e^{ik_z z}, \tag{23a}$$

$$u_\theta = (B_r (ik_z) K_1(br) + B_z b K_1(br))\, e^{ik_z z}, \tag{23b}$$

$$u_z = (B_0 (ik_z) K_0(ar) - B_\theta b K_0(br))\, e^{ik_z z}, \tag{23c}$$

and the stress components are

$$\tau_{rr} = 2\tilde{\mu}\left[B_0\left(\frac{b^2+k_z^2}{2}K_0(ar)+\frac{a}{r}K_1(ar)\right)\right.$$
$$\left.+B_\theta(ik_z)\left(bK_0(br)+\frac{1}{r}K_1(br)\right)\right]e^{ik_z z}, \quad (24a)$$

$$\tau_{rz} = \tilde{\mu}\left[-B_0(ik_z)2aK_1(ar)+B_\theta(b^2+k_z^2)K_1(br)\right]e^{ik_z z}, \quad (24b)$$

$$\tau_{r\theta} = \tilde{\mu}\left[B_r(ik_z)bK_0(br)+B_z b^2 K_0(br)\right]e^{ik_z z}, \quad (24c)$$

$$\tau_{\theta z} = \tilde{\mu}\left[-B_r k_z^2 I_1(br)-B_z b(ik_z)I_1(br)\right]e^{ik_z z}. \quad (24d)$$

Acknowledgements

The Acknowledgements come at the end of an article after Conflicts of interest and before the Notes and references.

Notes and references

1 R. Shuttleworth, *Proceedings of the physical society. Section A*, 1950, **63**, 444.
2 B. Andreotti, O. Bäumchen, F. Boulogne, K. E. Daniels, E. R. Dufresne, H. Perrin, T. Salez, J. H. Snoeijer and R. W. Style, *Soft Matter*, 2016, **12**, 2993–2996.
3 R. W. Style, A. Jagota, C.-Y. Hui and E. R. Dufresne, *Annual Review of Condensed Matter Physics*, 2017, **8**, 99–118.
4 J. Bico, É. Reyssat and B. Roman, *Annual Review of Fluid Mechanics*, 2018, **50**, 629–659.
5 S. Mora, T. Phou, J.-M. Fromental and Y. Pomeau, *Physical review letters*, 2014, **113**, 178301.
6 S. Tamim and J. Bostwick, *Soft Matter*, 2019, **15**, 9244–9252.
7 B. Saintyves, O. Dauchot and E. Bouchaud, *Physical review letters*, 2013, **111**, 047801.
8 X. Shao, J. Saylor and J. Bostwick, *Soft matter*, 2018, **14**, 7347–7353.
9 X. Shao, S. Fredericks, J. Saylor and J. Bostwick, *Physical review letters*, 2019, **123**, 188002.
10 J. Plateau, *Statique expérimentale et théorique des liquides soumis aux seules forces moléculaires*, Gauthier-Villars, 1873, vol. 2.
11 L. Rayleigh, *Proceedings of the London mathematical society*, 1878, **1**, 4–13.
12 L. Rayleigh, *Philosophical Magazine Series*, 1892, **34**, 177–180.
13 S. Mora, T. Phou, J.-M. Fromental, L. M. Pismen and Y. Pomeau, *Physical review letters*, 2010, **105**, 214301.
14 S. Ji and M. Guvendiren, *Frontiers in bioengineering and biotechnology*, 2017, **5**, 23.
15 O. A. Basaran, H. Gao and P. P. Bhat, *Annual Review of Fluid Mechanics*, 2013, **45**, 85–113.
16 R. Karyappa, T. Ching and M. Hashimoto, *ACS Applied Materials & Interfaces*, 2020, **12**, 23565–23575.
17 L. Mecozzi, O. Gennari, S. Coppola, F. Olivieri, R. Rega, B. Mandracchia, V. Vespini, A. Bramanti, P. Ferraro and S. Grilli, *ACS applied materials & interfaces*, 2018, **10**, 2122–2129.
18 E. Hannezo, J. Prost and J.-F. Joanny, *Physical review letters*, 2012, **109**, 018101.
19 A. L. Hazel and M. Heil, *Proceedings of the Royal Society A: Mathematical, Physical and Engineering Sciences*, 2005, **461**, 1847–1868.
20 P. Ciarletta and M. B. Amar, *Soft Matter*, 2012, **8**, 1760–1763.
21 M. Taffetani and P. Ciarletta, *Physical Review E*, 2015, **91**, 032413.
22 M. Taffetani and P. Ciarletta, *Journal of the Mechanics and Physics of Solids*, 2015, **81**, 91–120.
23 A. Pandey, M. Kansal, M. A. Herrada, J. Eggers and J. H. Snoeijer, *arXiv preprint arXiv:2012.08092*, 2020.
24 C. Xuan and J. Biggins, *Physical Review E*, 2017, **95**, 053106.
25 A. Giudici and J. S. Biggins, *Physical Review E*, 2020, **102**, 033007.
26 P. P. Bhat, S. Appathurai, M. T. Harris, M. Pasquali, G. H. McKinley and O. A. Basaran, *Nature Physics*, 2010, **6**, 625–631.
27 C. Xuan and J. Biggins, *Physical Review E*, 2016, **94**, 023107.
28 N. Cheewaruangroj, K. Leonavicius, S. Srinivas and J. S. Biggins, *Physical review letters*, 2019, **122**, 068003.
29 L. Wang, *International Journal of Solids and Structures*, 2020, **191**, 341–350.
30 S. Middleman, *Chemical Engineering Science*, 1965, **20**, 1037–1040.
31 G. H. Mckinley, *Annual Rheology Reviews*, 2005, 1–49.
32 D. T. Chen, Q. Wen, P. A. Janmey, J. C. Crocker and A. G. Yodh, *Annu. Rev. Condens. Matter Phys.*, 2010, **1**, 301–322.
33 X. Zhao, N. Huebsch, D. J. Mooney and Z. Suo, *Journal of applied physics*, 2010, **107**, 063509.
34 M. M. Fitzgerald, K. Bootsma, J. A. Berberich and J. L. Sparks, *Biomacromolecules*, 2015, **16**, 1497–1505.
35 T. Gao, G. J. Gillispie, J. S. Copus, A. K. Pr, Y.-J. Seol, A. Atala, J. J. Yoo and S. J. Lee, *Biofabrication*, 2018, **10**, 034106.
36 N. Reddy, R. Reddy and Q. Jiang, *Trends in biotechnology*, 2015, **33**, 362–369.
37 Y. Zhang, S. T. Ellison, S. Duraivel, C. D. Morley, C. R. Taylor and T. E. Angelini, *Bioprinting*, 2021, **21**, e00121.
38 P. Zhu, W. Yang, R. Wang, S. Gao, B. Li and Q. Li, *ACS applied materials & interfaces*, 2018, **10**, 36435–36442.
39 M. Tokita and K. Hikichi, *Physical Review A*, 1987, **35**, 4329.
40 T. Kajiya, A. Daerr, T. Narita, L. Royon, F. Lequeux and L. Limat, *Soft Matter*, 2013, **9**, 454–461.
41 S. Park, J. Bostwick, V. De Andrade and J. Je, *Soft Matter*, 2017, **13**, 8331–8336.
42 A. Wineman, *Mathematics and Mechanics of Solids*, 2009, **14**, 300–366.
43 S. Karpitschka, S. Das, M. van Gorcum, H. Perrin, B. Andreotti and J. H. Snoeijer, *Nature communications*, 2015, **6**, 1–7.
44 H. H. Winter and F. Chambon, *Journal of rheology*, 1986, **30**,

367–382.

45 F. Chambon and H. H. Winter, *Journal of Rheology*, 1987, **31**, 683–697.

46 H. Kibbelaar, A. Deblais, F. Burla, G. Koenderink, K. Velikov and D. Bonn, *Physical Review Fluids*, 2020, **5**, 092001.

47 J. Eggers, M. A. Herrada and J. Snoeijer, *Journal of Fluid Mechanics*, 2020, **887**, A19.

48 R. Christensen, *Theory of viscoelasticity: an introduction*, Elsevier, 2012.

49 F. Mainardi and G. Spada, *The European Physical Journal Special Topics*, 2011, **193**, 133–160.

50 K. D. Papoulia, V. P. Panoskaltsis, N. V. Kurup and I. Korovajchuk, *Rheologica Acta*, 2010, **49**, 381–400.

51 A. Bonfanti, J. L. Kaplan, G. Charras and A. J. Kabla, *Soft Matter*, 2020, **16**, 6002–6020.

52 R. Gillette and D. Dyson, *The Chemical Engineering Journal*, 1972, **3**, 196–199.

53 J. Bostwick and P. Steen, *Journal of fluid mechanics*, 2010, **647**, 201–219.

54 M. Reiner, *Physics today*, 1964, **17**, 62.

55 V. Normand, D. L. Lootens, E. Amici, K. P. Plucknett and P. Aymard, *Biomacromolecules*, 2000, **1**, 730–738.

56 A. Wahlsten, M. Pensalfini, A. Stracuzzi, G. Restivo, R. Hopf and E. Mazza, *Biomechanics and modeling in mechanobiology*, 2019, **18**, 1079–1093.

57 C. Storm, J. J. Pastore, F. C. MacKintosh, T. C. Lubensky and P. A. Janmey, *Nature*, 2005, **435**, 191–194.

58 F. Charru and P. de Forcrand-Millard, *Hydrodynamic Instabilities*, Cambridge University Press, 2011.

59 C. S. O'Bryan, T. Bhattacharjee, S. L. Marshall, W. G. Sawyer and T. E. Angelini, *Bioprinting*, 2018, **11**, e00037.